Resolution dependence of cross-tropopause ozone transport over east Asia

M. L. Büker, Matthew H. Hitchman, and Gregory J. Tripoli
Department of Atmospheric Sciences, University of Wisconsin, Madison, Wisconsin, USA

R. B. Pierce, E. V. Browell, and M. A. Avery
NASA Langley Research Center, Hampton, Virginia, USA

Received 5 March 2004; revised 17 June 2004; accepted 13 September 2004; published 4 February 2005.

[1] Detailed analysis of mesoscale transport of ozone across the tropopause over east Asia during the spring of 2001 is conducted using regional simulations with the University of Wisconsin Nonhydrostatic Modeling System (UWNMS), in situ flight data, and a new two-scale approach to diagnosing this ozone flux. From late February to early April, synoptic activity regularly deformed the tropopause, leading to observations of ozone-rich (concentration exceeding 80 ppbv) stratospheric intrusions and filaments at tropospheric altitudes. Since model resolution is generally not sufficient to capture detailed small-scale mixing processes, an upper bound on the flux is proposed by assuming that there exists a dynamical division by spatial scale, above which the wind conservatively advects large-scale structures, while below it the wind leads to irreversible transport through nonconservative random strain. A formulation for this diagnosis is given and applied to ozone flux across the dynamical tropopause. Simulations were chosen to correspond with DC-8 flight 15 on 26–27 March over east Asia during the Transport and Chemical Evolution Over the Pacific (TRACE-P) campaign. Local and domain-averaged flux values using this method agree with other numerical and observational studies in similar synoptic environments. Sensitivity to numerical resolution, prescribed divisional spatial scale, and potential vorticity (PV) level is investigated. Divergent residual flow in regions of high ozone, and PV gradients tended to maximize flux magnitudes. We estimated the domain-integrated flow of ozone out of the lowermost stratosphere to be about 0.127 Tg/day. Spectral analysis of the wind field lends support for utilization of this dynamical division in this methodology.

Citation: Büker, M. L., M. H. Hitchman, G. J. Tripoli, R. B. Pierce, E. V. Browell, and M. A. Avery (2005), Resolution dependence of cross-tropopause ozone transport over east Asia, *J. Geophys. Res.*, *110*, D03107, doi:10.1029/2004JD004739.

1. Introduction

[2] Stratosphere-troposphere exchange (STE) has been shown to play a significant role in atmospheric redistribution of ozone and other trace gases, and thus has been the focus of a significant body of literature. *Holton et al.* [1995] and *Stohl et al.* [2003] provide comprehensive reviews of the current state of research on STE. With the advent of increased computational power and reasonable initialization of meteorological variables and ozone profiles, direct computation of ozone flux across the tropopause at high resolution seems to be an attainable goal. However, there is some difficulty in determining what exactly this computation represents; indeed, there are still some theoretical problems regarding how flux through a material surface is envisioned, especially in cases where diabatic heating is negligible. Several recent studies [*Wirth and Egger*, 1999; *Sigmond et al.*, 2000; *Stohl et al.*, 2003] have argued that a Lagrangian approach must be used in order to obtain realistic profiles of mass exchange. However, the bulk of significant values in these studies were attributed to diabatic heating (such as latent heating) along a trajectory, resulting in mass "flowing" across the tropopause (or the tropopause reforming above the mass). Although diabatic heating can contribute significantly to STE, one must be careful how localized diabatic heating is represented. It would seem that high-resolution simulations with horizontal resolutions on the scale of convection, as well as very accurate radiative transfer formulations, would be needed to accurately compute the distribution of flux due to diabatic heating in such cases. Furthermore, in the case of strong deformation of the tropopause, resolved Lagrangian changes in potential temperature are not necessarily existent, yet these methods show that STE still occurs in these regions. *Wirth and Egger* [1999] attribute this to explicit and implicit diffusion, which "does not necessarily represent a physical process present in the real atmosphere." Yet it is known that at some smaller scale

there is transport across the tropopause, usually attributed to "turbulent mixing." A question to be asked in conjunction with this problem is what spatial-scale marks the transition between isentropic, potential vorticity (PV) conserving flow, which is fundamentally advective, and "mixing" at smaller scales, where transport is defined in terms of chaotic advection, turbulence, or molecular diffusion. Here a new two-scale method is proposed which may be useful in determining a more physically based calculation of STE.

[3] A description of the model specifications is provided in section 2, followed by an explanation of the two-scale method, along with our definition of the tropopause in section 3. Section 4 describes a case study which coincides with flight 15 on 26 March 2001 during the TRACE-P (Transport and Chemical Evolution over the Pacific) campaign when strong STE was forecast to occur [*Jacob et al.*, 2003]. In section 5 the two-scale method is applied to this case, with the emphasis on sensitivity to horizontal resolution, spatial scale and PV level. Comparison of flux profiles and values to similar studies are made as well. Results are also compared to in situ measurements of ozone and horizontal winds. A discussion of the results and the direction of future work is given in section 6.

2. Model Specifications and Initialization

[4] The UWNMS is a multiscale numerical weather prediction model, with applicability to processes on scales ranging from meters to global (general circulation model (GCM)) resolutions [*Tripoli*, 1992a, 1992b]. The model has been used in recent field campaigns such as the Polar Ozone Loss in Arctic Regions in the Summer (POLARIS) and the Sage III Ozone Loss and Validation Experiment (SOLVE), in addition to the TRACE-P experiment [*Hitchman et al.*, 1999, 2003, 2004]. The UWNMS has also been combined with a global isentropic model [*Johnson et al.*, 1993] and a detailed chemistry package from the Langley IMPACT model [*Eckman et al.*, 1995] to create the Regional Air Quality Modeling System (RAQMS) [*Pierce et al.*, 2003].

[5] We initialize the meteorological fields with aviation model (AVN) analyses from the National Centers for Environmental Prediction with $1^\circ \times 1^\circ$ horizontal resolution, interpolated to varying model grids. Three dimensional ozone profiles of the same resolution are obtained from simulations with the RAQMS and also interpolated [*Pierce et al.*, 2003]. After initialization, the boundary conditions are forced by subsequent analyses, linearly interpolated in time and space with updates every 6 hours, while the model interior is allowed to evolve within the parameters of the physics. We varied the horizontal resolution in increments of 10 km from 20 km to 100 km. Standard meteorological fields (winds, temperature, pressure, water vapor, rainfall) are archived at 30 minute intervals, with simulations spanning 2.5 days. The model time step was 60 s. The model domain was centered over the East China Sea, 3000 km on a side. Vertical resolution was kept constant for all simulations at 400 meters, with the top of the domain extending to 24 km. Rayleigh friction sponge layers were implemented on the sidewalls (5 grid points) and top (10 grid points) of the domain.

3. Two-Scale Method and Tropopause Definition

[6] In determining the flux of mass across a dynamical material surface (such as the tropopause), we distinguish the conserved advection of the material surface (e.g., a PV isopleth) by the large-scale wind field, from the "smaller-scale" resolved nonconservative motions contributing to irreversible mixing. *Wei* [1987] made the assumption in their study that small-scale mixing "can rapidly modify the PV of air parcels," and that, given the fine-grain structure of the distribution of PV [*Hoskins et al.*, 1985], "any stratospheric air entering a fold is assumed to be irreversibly transferred to the troposphere" [e.g., *Shapiro*, 1980]. In our two-scale method it is assumed that, at some point, an intruding PV surface will become distorted enough at small scales to be considered irreversibly "mixed" with tropospheric air. Below the scale of the Rossby radius ($\sim$500–1000 km near the tropopause), divergent flows are increasingly important.

[7] In the cases presented here, we separate scales by creating low-pass filtered winds and a residual. This is done by applying a 1-2-1 bilinear smoothing operator at each altitude, with a response function given by *Haltiner and Williams* [1980]:

$$R_m = \cos^{2m}\frac{(\pi\Delta x)}{L_{pr}}, \tag{1}$$

where R is the response ($0 < R < 1.0$), m is the number of passes, Δx is the horizontal resolution. L_{pr} is the prescribed spatial scale of separation, where scales of motion above L_{pr} are kept in the smoothed field, while most of the energy associated with scales near and below L_{pr} are retained as the "residual" field. The response profile as a function of L_{pr} and m for differing horizontal resolutions (e.g., Δx = 30, 60, and 120 km) reveals that to obtain the same signal at a given L_{pr} for varying Δx, the number of passes must be increased by about $(\Delta x_2/\Delta x_1)^2$, where $\Delta x_2 < \Delta x_1$. For example, at 30 km resolution, 16 passes are required to give the same response as four passes at 60 km resolution.

[8] The response profile is steeper at higher horizontal resolutions for the same number of passes, including a greater percentage of the total wind in the smoothed field. We acknowledge that there exist filters with a sharper response function [e.g., *Barnes*, 1973]. However, we surmise that motions contributing to the flux occur over a range of scales. Given that modes of flux at lower resolutions will be more poorly resolved at smaller length scales, more signal at higher L_{pr} should be included, resulting in a broader response spectrum. Table 1 shows the number of passes for each combination of Δx and L_{pr}, given a target response of the filtered field at 0.1. This value was chosen to ensure a significant component of the residual field (or, conversely, to ensure a very small component of sub-L_{pr} motions in the smoothed field) throughout the range of chosen length scales, even at coarse resolutions.

[9] This smoothed wind field is then used to compute the PV field. We define the tropopause as a surface of this smoothed PV, and define ozone fluxes through this surface

Table 1. Number of Bilinear Passes Needed to Obtain $R(L_{pr}) \leq 0.1$ as a Function of Δx

	Horizontal Resolution					
L_{pr}	20 km	30 km	40 km	50 km	75 km	100 km
200	23	10	6	4	2	-
300	53	23	13	9	4	2
400	93	42	23	15	7	4
500	146	65	37	23	10	6
600	210	93	53	34	15	9
800	373	166	93	60	27	15
1000	583	259	146	93	42	23

as the local STE. The ozone field is left unaltered. In making this assertion, we assume that PV structures smaller than the prescribed scale have been deformed to the point of irreversible entanglement with tropospheric air. Thus this material is already considered mixed into the troposphere.

[10] We utilize a "modified direct method" approach [after *Wirth and Egger*, 1999] to computing flux across the tropopause by starting with the magnitude of the flow normal to the given PV surface:

$$\mathbf{V}_{\perp} = (\mathbf{V} \cdot \mathbf{n})\mathbf{n}, \tag{2}$$

where

$$\mathbf{n} = \frac{\nabla P}{|\nabla P|}. \tag{3}$$

We then assume the conserved advection of the tropopause surface to be accounted for by the smoothed wind field:

$$\mathbf{V}_{\mathbf{s}\perp} = (\mathbf{V}_{\mathbf{s}} \cdot \mathbf{n})\mathbf{n}, \tag{4}$$

[11] The difference between the two wind fields is then computed and multiplied by the full (unsmoothed) ozone field (volumetric mixing ratio) to give an instantaneous ozone flux through the PV surface:

$$\mathbf{F}_{O_3} = n_{air} m_{O_3} \times \mathbf{V}_{\mathbf{m}\perp}, \tag{5}$$

where n_{air} is air number density, m_{O_3} is volumetric mixing ratio for ozone, and $\mathbf{V}_{\mathbf{m}\perp} = \mathbf{V}_{\perp} - \mathbf{V}_{\mathbf{s}\perp}$.

[12] By using the full ozone field, we are retaining the small-scale variability of both the tracer and the residual normal component of the wind to obtain the fine structure of the flux normal to the smoothed PV surface, circumventing the difficulty of uncertainty in gradient calculations of a noisy PV field. It is recognized that the range of delimiting scales of separation (as well as the range of PV values for the tropopause) seem somewhat arbitrary. However, the chosen values cover much of the meso-β (20–200 km) to meso-α (200–2000 km) [*Orlanski*, 1975] scale range, where it is hypothesized the bulk of the flux takes place. This two-scale approach is thus summarized in the schematic in Figure 1. The velocity field is smoothed to a given response at a prescribed spatial scale. A "smoothed" PV field is generated from this altered wind field, which in turn is assumed to account for the advection of the new PV field. The difference of the smoothed-PV-normal velocity vectors between the smoothed and unsmoothed wind fields accounts for the spatial variability of **V** about the material surface. This variability provides the chaotic stirring of the surface which eventually results in irreversible mixing, and diagnosed as material flux across the tropopause.

4. Case Study of TRACE-P Flight 15: 26 March 2001

4.1. Synoptic Overview

[13] When using a dynamical definition of the tropopause, a lower, more tropospheric value of PV generally tends to have a more complex structure. In this section, we chose a value toward the lower end of generally accepted values for the tropopause (1.3 PVU). This value tends to maximize visualization of structural evolution of the tropopause while keeping noise in the PV field from confusing the picture. The sequence of images in Figure 2 shows how the 1.3 PVU isosurface, shaded by pressure, evolved during the period between 12Z 25 March and 12Z 27 March 2001. The range in pressure for this PV surface was quite broad (~100–650 hPa). Overlayed are contours of mean sea level pressure. At 1200 UT on the 25th (Figure 2a), a deep polar trough (indicated by darker shading, or higher pressure, of the PV surface) extended north of the Korean peninsula, while a subtropical upper front (indicated by a sharp north-south contrast in shading of the PV surface) extended roughly east-west across mainland China. At the surface, two areas of low pressure straddled Japan to the north and south, with the northern low favorably positioned relative to the upper trough for rapid cyclogenesis. By 00Z on the 26th (not shown), the northern low had deepened considerably while the upper trough elongated and sharpened downward (higher pressure) toward the south and east. This feature was quite pronounced when viewed from the southwest, as in Figure 3. Indeed, this was a time of strong STE. Also of note in Figure 3 is the formation of dislocated PV filaments below the subtropical tropopause break. The trough continued to elongate through 12Z on the 26th (Figure 2b), with the PV gradient weakening somewhat at the western flank of the trough. The surface low, at this time over the Sikhota Alin mountains (north of Vladivostok), had occluded and begun to fill, while the other area of low pressure had moved to the east of Japan. The east-west lineament of the sharp meridional PV gradient continued

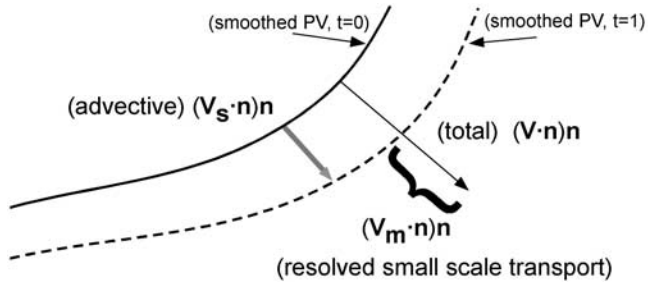

Figure 1. Schematic of the two-scale approach to flux calculation. The solid and dashed lines delineate the advection of the PV isosurface with the smoothed normal wind and the flux represented by the difference in the normal wind between the smoothed and unsmoothed wind field.

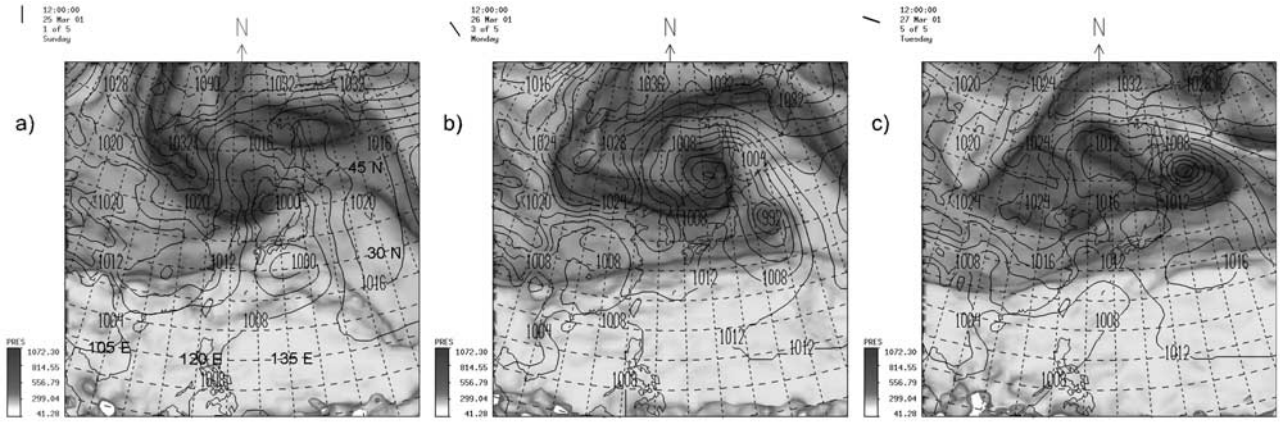

Figure 2. Synoptic progression of the lowermost tropopause represented by the 1.3 PVU isosurface. This surface is shaded by pressure with the index in the lower left of each panel (darker for higher pressure, lighter for lower pressure). Mean sea-level pressure is also contoured every 4 hPa. The time periods represented are (a) 1200 UT 25 March 2001, (b) 1200 UT 25 March 2001, and (c) 1200 UT 27 March 2001.

into the 27th (Figure 2c), when a sortie was scheduled for TRACE-P. Several significant folds of the tropopause were occurring during the flight: one area just south of Japan, another over the southern Yellow Sea, and yet another beginning to redevelop over the Korean Peninsula. In short, the tropopause had very complex structure throughout the simulation. Significant intrusions of stratospheric air were tested with our new flux methodology.

4.2. Flight Goals and Results

[14] One of the main objectives of this flight was to examine the tropopause fold under the northern flank of a tropospheric jet streak. The fold was forecast by several models to be located at the southern edge of the Yellow Sea (30−−32°N, 125°E) at an altitude of about 8–10 km. A satellite photo with the flight track superimposed is shown in Figure 4, where a cloud streak is indicative of the strong jet stream. On-flight nowcasting at higher resolution with the UW-NMS predicted the fold to extend from ∼8 km altitude at the southern flank to ∼10 km at the top of the depression. Figure 2c shows the sharp PV gradient over the East China Sea on 27 March 2001. A constant-altitude leg from 0400–0500 UT at ∼10 km was incorporated into the flight plan. Figure 5 shows curtain profile of ozone [*Browell et al.*, 2003] during the flight. The pronounced feature of enhanced ozone mixing ratio is clearly evident with structure extending down to about 7.5 km at the southern flank (about 24°N, 127°E), with a stronger feature from 9.5–12 km in the northern half of the leg (about 34°N, 125°E). Upon descent from this leg, but still traveling further north, the flight still followed a significant ozone gradient down below 7 km at around 0600 UT. In addition, a smaller ozone filament was observed during the last portion of the flight, near and north of southwestern Japan, or about 33–35°N, 129–−135°E.

4.3. Model and Flight Data Comparison

[15] Much of the significant wind and ozone structure observed by the DC-8 was captured in the UW-NMS simulations (Figure 6). Both of the largest tropopause folds seen in the lidar data (0000–0100 UT, 0700–0800 UT) are seen in situ (*Avery et al.* [2001]; see http://www-gte.larc.nasa.gov/trace/TP_Avery_Vay_Instrument.htm; http://cloud1.arc.nasa.gov/solveII/instrument_files/O3.pdf) and in the UW-NMS ozone fields (Figure 6c). Overall, there is fairly good agreement between the observed and model data in both typical magnitudes of the intrusions and their general location. There is also general agreement with the along-track wind profiles between the DC-8 and the UWNMS. The zonal wind component agrees quite well, as shown in Figure 6a. At the flight level (∼10 km) there was a complex

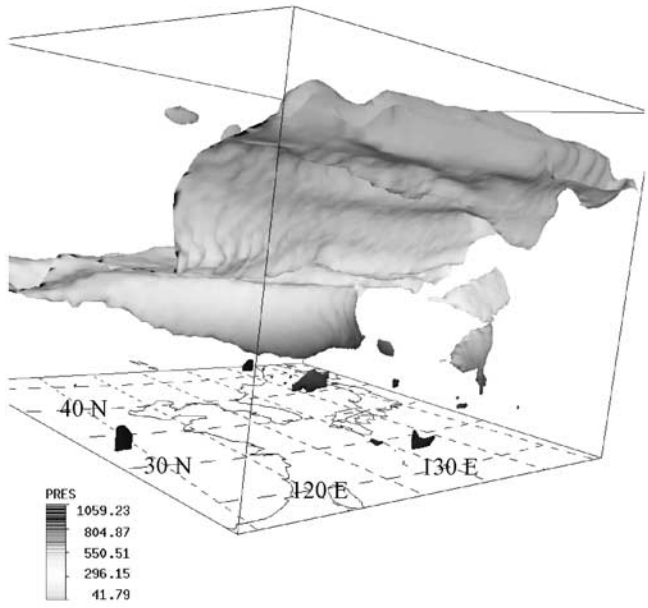

Figure 3. The 1.3 PVU isosurface at 1630 UTC 26 March, viewing from the southwest, colored by pressure (red for higher pressure, blue for lower pressure). Note the dislocated features in the mid-troposphere in the south-eastern quadrant of the domain. See color version of this figure at back of this issue.

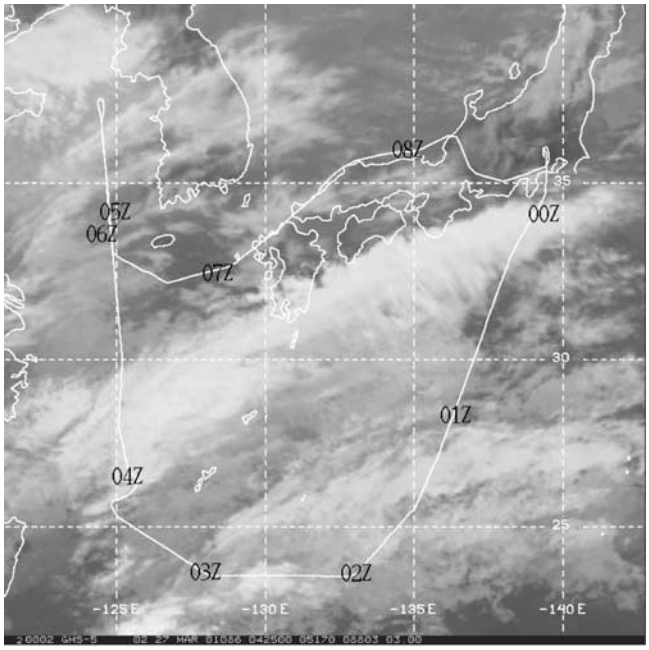

Figure 4. Horizontal projection of DC8 TRACE-P flight 15 during 2330 UT 26 March to 0830 UT 27 March 2001 (0830 to 1730 local time), superimposed on an infrared image from the GMS-5 satellite at 0425 UT (1325 local time). Time stamps provide the location of the DC-8 at each hour.

jet structure extending across this area (Figures 2c and 6a). There are slight discrepancies in exact location of the intrusions.

[16] At the lowest altitudes (as indicated by wind speeds near zero) lower tropospheric ozone values are somewhat too low in the UWNMS. On the boundary layer legs of the flight, the UWNMS underpredicts ozone levels. This could be due to insufficient vertical resolution in the lowest layers, resulting in less mixing with higher values aloft. One of the larger descrepancies in the upper troposphere/lower stratosphere is in the first high altitude excursion around 0000–0100 UTC. Here the UWNMS has a significant peak in ozone which is broader and reduced in the in situ data. However, one can see from the lidar data at this same time that a significantly larger ozone maximum was located less than 1 km above the aircraft. It is likely that flux calculations based on the model wind and ozone fields are not strongly dependent upon slight deviations in locations of significant features.

5. Ozone Flux Analysis

5.1. Resolution Dependence of Modeled Flux

[17] The extent of sensitivity tests for this case study are outlined in Table 1. Six horizontal resolutions were tested (20, 30, 40, 50, 75 and 100 km), varying also the prescribed spatial-scale L_{pr} (200–1000 km) and the PV level (0.9–2.4) at which the flux was computed. Again, in order to achieve a consistent response $R(L_{pr}, \Delta x)$ (R = 0.1 was chosen) for a given L_{pr}, the number of passes necessary with the bilinear filter grows exponentially with increasing L_{pr} and horizontal resolution. We examined the spatial distribution of instantaneous flux, domain-integrated instantaneous flux, and spatiotemporal integrated flux for the various combinations of L_{pr}, Δx, and PV.

5.2. Variation of Instantaneous Flux Distribution

[18] For the purposes of looking at how the flux varies in 3-D, we chose a fixed L_{pr} of 500 km, while computing the values at all the PV levels mentioned above. At the highest resolution, the calculation got quite noisy. Smoothing was applied to the flux field to the same degree as to the wind field, with similar reasoning for the filter applied in the work of *Barnes et al.* [1996], where it was desirable to filter out gravity waves in the Q vector analysis. (We show later that this smoothing has a relatively small effect on the domain-integrated instantaneous flux.)

[19] Figure 7 shows a four-panel rendering of the six simulations at varying resolution. Plotted is the −10 unit flux isosurface (1 unit = 1×10^{12} mol O_3/cm^2–s) at 1630 UTC on 26 March, with resolution increasing from left to right (50, 40, 30 and 20 km). Immediately apparent was the lack of features for this flux magnitude at low resolutions (75 and 100 km, not shown). Only a few grid points (not visible) in the far eastern domain exceeded the −10 unit threshold at 100-km resolution, with little increase in flux going to 75-km resolution. Only at 50-km does the expected region of flux (in the region of the deep fold) begin to show a significant isosurface. Referring back to Figure 2b, the areas of strongest flux correlate with the deep polar trough over the Sea of Japan, the subtropical tropopause break south of Japan. The isolated filament in Figure 3 also correlates with a strong area of flux (the patch south of Japan in Figures 7c and 7d).

5.3. Instantaneous Flux Profiles

5.3.1. Sea of Japan, 1630Z 26 March

[20] At 1630Z in the simulation the sharp PV intrusion across the Sea of Japan reached peak intensity. Figure 8a

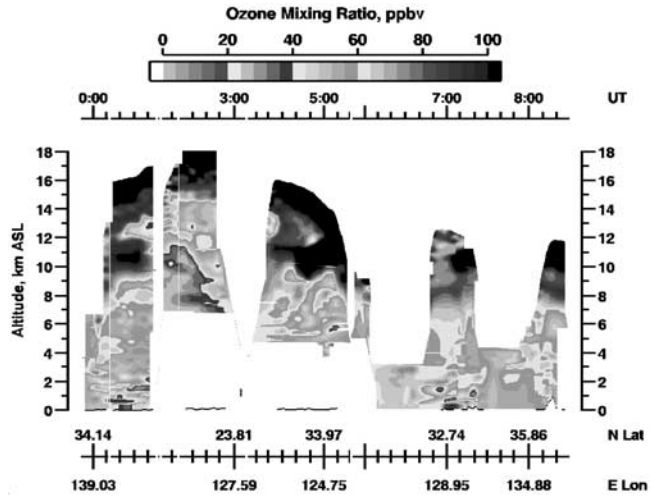

Figure 5. Time-height section of Langley DIAL ozone mixing ratio in ppbv for flight 15. Note the pronounced ozone intrusions at 0000–0100 UT, 0400–0500 UT, and 0700–0800 UT. See color version of this figure at back of this issue.

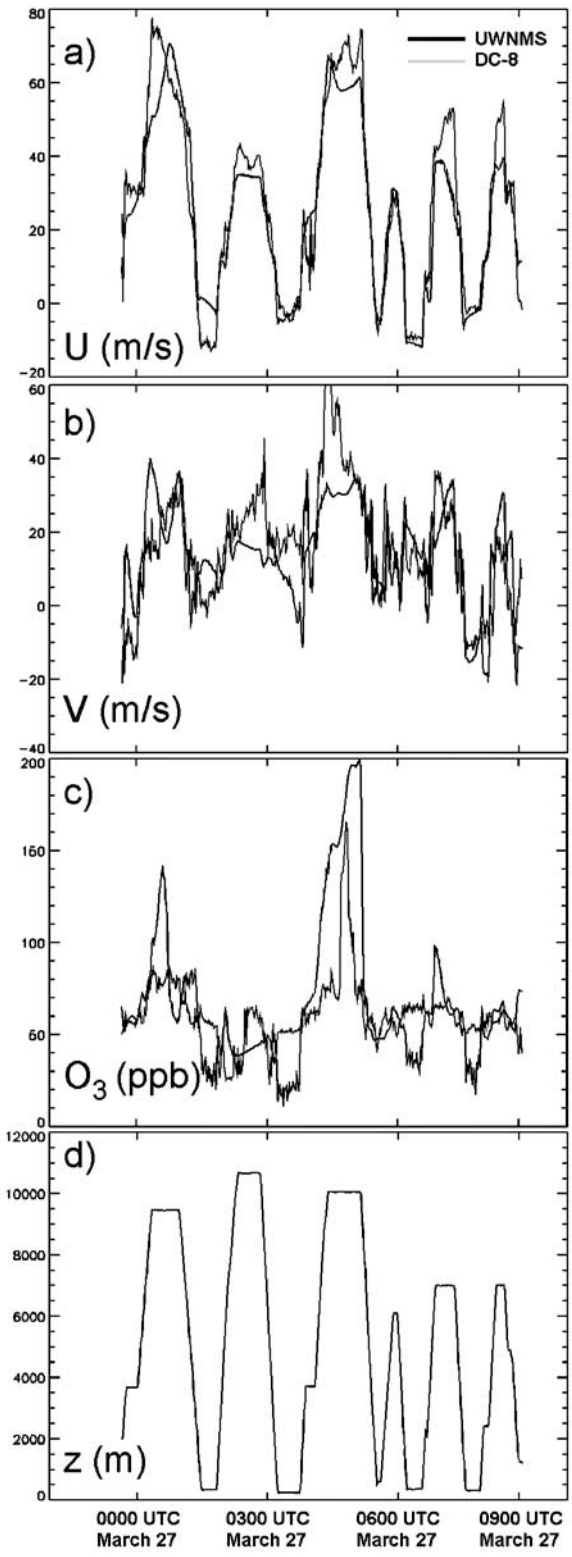

Figure 6. Model (black) and in situ (gray) flight track comparison of (a) zonal wind (knots), (b) meridional wind (knots), (c) ozone (ppbv), and (d) altitude (meters) for DC-8 flight 15.

shows PV and ozone flux contours at z = 5.1 km, with ozone mixing ratio shaded from 0 ppb (whitest) to 200 ppb (darkest). The highest (negative) values of flux are occurring along the rear (southwestern) flank of the trough, maximizing near the base. This seems intuitive; however, the diagnostic reveals a small positive flux on the forward (northeastward) flank. We also superimpose the residual (full - smoothed) wind at 5.1 km. One can see that along the southwestern flank several factors come together: first, the ozone maximizes in this part of the trough; second, residual winds are the strongest; and third, there is a divergent pattern in the residual wind in the same region. Looking to the northeast (forward flank) a convergent pattern with much lighter winds and smaller ozone concentration coincides with smaller, positive flux values. The southward extension away from the trough is an artifact of the smoothing of the flux field. The filament associated with the PV fold south of Japan (Figures 8a and 2b) does not have a divergent residual wind field. This is likely the reason for the local flux being negligible at that time. Divergence in the residual flow that is normal to the PV gradient is akin to a deformation that weakens the gradient. Flux due to nonconservative motions would tend to maximize in a deformation with this orientation.

[21] Vertical profiles, shown in Figures 9a–9b show a complementary view of the relationship between PV, ozone, the residual wind and ozone flux values. A vertical slice along 140°E shows ozone flux maximizing about the southern flank of the intrusion. An interesting aspect was that the flux maximizes at the altitude of the middle of the filament, rather than toward the bottom (Figure 9a), likely due to turbulence on the periphery of the jet. Aligning the slice along 39°N and superimposing the residual wind shows a general "down and out" flow along the filament with flux maximizing at the east-central portion of the intrusion (Figure 9b). On the western flank there appears to be a positive flux according to the wind field (residual convergence into the filament) in this vertical slice. However, the horizontal residual divergence (shown in Figure 8a) is greater in that vicinity shown in 9b. Again, the isolated filament of higher PV and moderate ozone concentration south of Japan between 6 and 9 km altitude (shown in Figures 8a and 9a) does not exhibit significant flux at this time (likely due to a slight residual convergent flow in the region). However, as shown in the following section, this feature evolves to generate appreciable flux.

5.3.2. South of Japan, 0800 UT 27 March

[22] Ozone, ozone flux, PV and residual winds in the UWNMS are shown for 0800 UT on 27 March in Figure 10. Outward flux in the isolated filament south of Japan is again coincident with a divergent residual flow and a relatively high ozone concentration. Note that the maximum flux is not coincident with the local maximum in PV at this height level (4.6 km). This feature later "rejoined" the stratosphere as the simulation continued, as a separate downward extension of the tropopause developed in the vicinity of the filament (not shown). This highlights the need for computation of flux on isolated areas of PV and high ozone, at least on structures with length scales above the middle meso-β range (around 100 km), as material contained in such

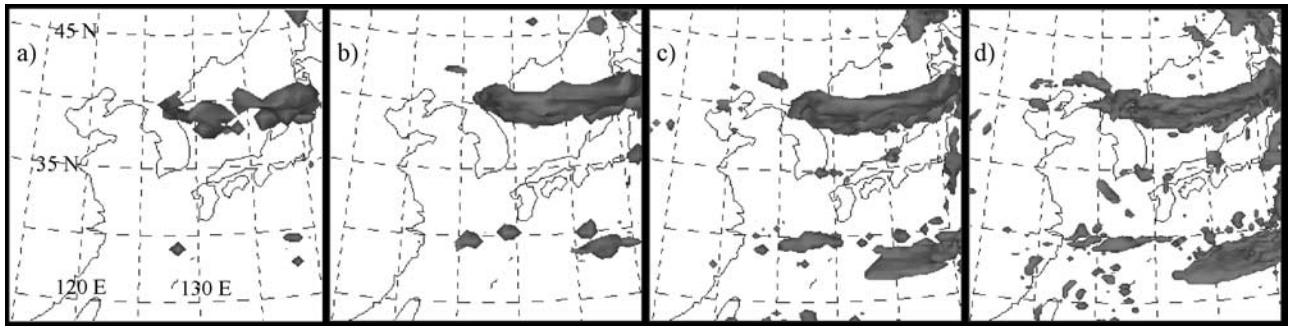

Figure 7. Instantaneous flux values across the 1.5 PV isosurface calculated with the two-scale method in the UWNMS at varying horizontal resolutions. The −10 unit isosurface (1 unit = 1×10^{12} molecules O_3/cm^2-s) is shown for 1630 UT 26 March for a horizontal resolution of (a) 50 km, (b) 40 km, (c) 30 km, and (d) 20 km.

"isolated" filaments is not necessarily irreversibly transported by that time.

5.4. Domain-Integrated Flux Profiles: Three-Fold Sensitivity

5.4.1. Horizontal Resolution Sensitivity

[23] Figure 11 shows a sequence of spatially integrated net flux in the simulation versus time at varying horizontal resolutions. For this example, the PV surface and separation scale length is kept constant at 1.5 PVU and 500 km, respectively. For almost all resolutions, however, two areas of highest negative flux appear during roughly the same time periods: a long-duration event during 1500–2300 UTC, and a shorter duration event around the time of the DC-8 flight (0500–1100 UTC). There appears to be a dramatic shift in magnitude at around $\Delta x \sim 40-50$ km, as the average negative flux values (during the maxima) increase by about a factor of five. Values increase somewhat in magnitude at higher resolutions as well. There is also an overall shift in the general direction of the flux going from upward at $\Delta x = 75$ km to downward at $\Delta x = 40$ km, changing from generally troposphere to stratosphere transport (TST) to stratosphere to troposphere transport (STT). This phenomenon is discussed further in section 5.4. It is interesting to note that temporal breadth of the intense negative flux event minimizes at 30 and 40 km resolution. It is possible that at too high of a horizontal resolution, sub-"PV-advecting" motions may have rapid fluctuations that can result in an overestimation of their stirring impact. This overestimation is surmised to occur due to "multiple accounting" of flux across a given PV surface.

[24] Given a transition from a purely chaotic flow to a self-similar turbulent cascade, accounting of flux due to residual winds normal to a PV surface may begin to become redundant. In purely chaotic flow, material lines may become stretched or contracted, increasing or decreasing the potential for flux across the surface. In the transition to turbulence, self-similar enstrophy cascade to smaller scales will invariably stretch material lines past the point of irreversibility. Any motions included after this transition do nothing further to enhance the flux. It may be the case that much of the variation in the residual flow at scales below 30–40 km is due to turbulent motion.

5.4.2. Separation Scale Sensitivity

[25] To test sensitivity to the prescribed spatial scale of separation, 30 km horizontal resolution and 1.5 PVU were kept as constants, while ranging L_{pr} from 200 km to 1000 km (Figure 12). A division is immediately apparent between $L_{pr} = 400$ and $L_{pr} = 500$ km. When L_{pr} is larger, the first negative flux event is picked up definitively, while the second event is only barely discernable at $L_{pr} = 500$ km. This would be indicative of deep, broad mixing where motions in the lower to middle mesoalpha range (from 200–400 km) are contributing to most of the flux, with $L_{pr} = 500-600$ km maximizing the instantaneous flux values. Finer-scale motions, where $L_{pr} \leq 400$ km, capture the second flux event much more clearly, and extend the temporal range of the event (to beyond 1200 UTC 27 Mar) as well. Here the flux is maximized at around $L_{pr} = 300$ or 400 km. Comparing with Figures 8 and 10, the ratio of spatial scale of the two intrusions is roughly the same as the L_{pr} ratios here. This range of scales is consistent with the spatial scales used in the work of *Dethof et al.* [2000], where "cutoff" scales were chosen in contour advection surgery. In that study, smaller-scale structures were removed by merging or disconnecting contours when they approach closer than the prescribed spatial scale. Net flux was maximized in their sensitivity study at a value of about 320–380 km for the cutoff scale.

5.4.3. Sensitivity to PV Level

[26] In Figure 13, the horizontal resolution is again kept at 30 km, L_{pr} is maintained at 500 km, and PV is varied from 0.9 to 2.4 PVU. The geometric range of this PV "slab" is, on average, about 3.5 km and is centered near 11 km (not shown). The extent of calculated flux across this dimension is directly indicative of the depth of mixing in an event. In addition, the net flow of ozone through the lowermost stratosphere can also be inferred from a vertical flux divergence perspective. (This is discussed further in section 5.6.) At low PV values (0.9, 1.1 PVU), the two flux events are nearly indistinguishable, with instantaneous flux values holding between 5 and 7×10^{28} molecules/s for the period from 1500 UTC 26 Mar to 1200 UTC Mar 27. A break between the two events starts to become discernible at 1.3 and 1.5 PVU. At 1.8 PVU, the first event is isolated in time, with the second event not clearly visible. Flux values at 2.1 and

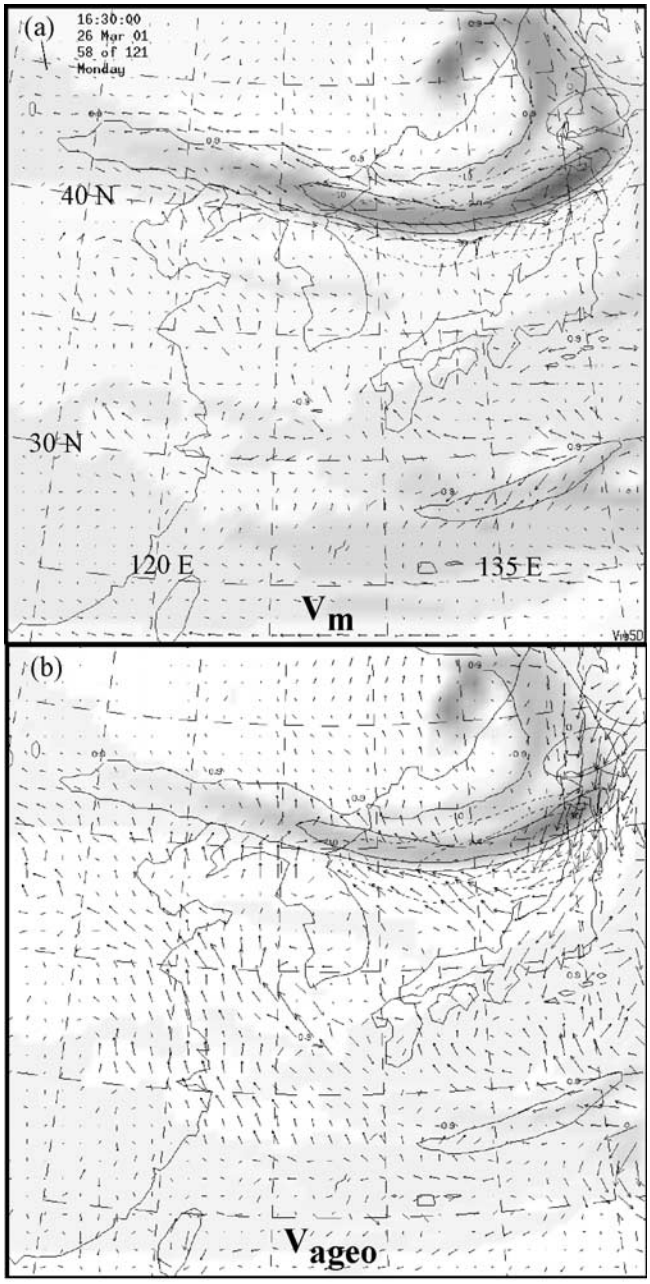

Figure 8. (a) UWNMS simulation of the TRACE-P domain at 1630 UT, showing ozone shaded darkest (200 ppbv) to lightest (0 ppbv), PV (solid contours of 0.9 and 2.4 PVU), ozone flux (dashed contours, 0 to -30 units (1 unit = 1×10^{12} mol O_3/cm^2-s)), and residual winds (vectors) at z = 5.1 km. (b) As in Figure 8a, but with ageostrophic wind vectors.

2.4 PVU are significantly muted for the first event, while the second event holds fairly steady in magnitude, around -2×10^{28} molecules O_3/s.

[27] These PV values being used for the definition of the tropopause are relatively low compared to other studies, where the tropopause is rarely defined below 2 PVU. This may be due in part to resolution capability, where differentiation between small values of PV may be difficult to obtain. In addition, this study is focusing on the very edge of the stratosphere where the "permeability" is less resistant to mixing. It has become apparent in this study that stratospheric-like structures in the PV field, even at values less than 0.9 PVU, are ubiquitous in a layer near and parallel to the tropopause, especially at higher resolutions.

5.5. Spatiotemporally Integrated Flux Sensitivity

[28] The sensitivities to the flux calculation, when considering the aggregate flux throughout the domain for the duration of the simulation, can be summarized by contouring this total flux on an L_{pr} versus grid at the varying horizontal resolutions (Figure 14). Again, this diagnostic

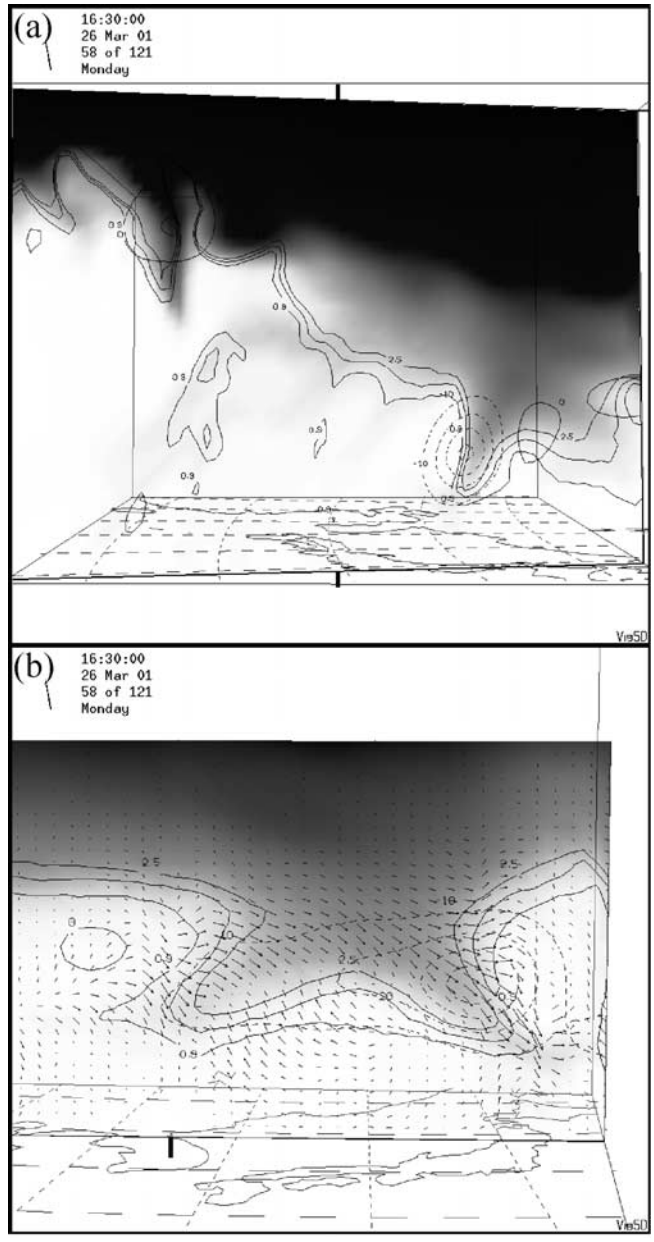

Figure 9. (a) As in Figure 8a, except viewing a vertical slice along 140°E, seen from the east. (b) As in Figure 9a, but showing a vertical slice along 39°N as seen from the south, with residual winds superimposed and a closer view. Note the residual flow down and out of the eastern downward intrusion.

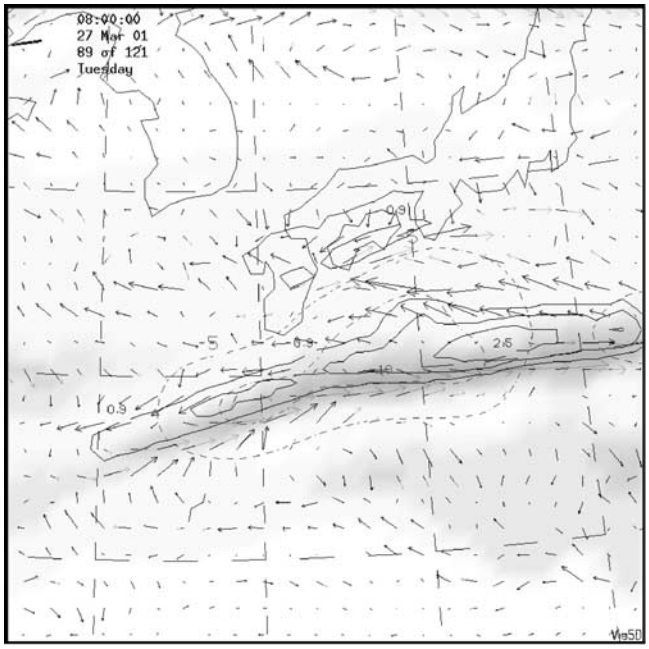

Figure 10. (a) As in Figure 8a, but at 0800 UT 27 March and z = 4.6 km, with flux contoured every 5 units, with residual wind vectors superimposed and a closer view.

predicts positive upward fluxes for $\Delta x > 50$ km. At $\Delta x = 50$ km, a rapid transition occurs, with net positive flux at higher L_{pr} and lower PV, with downward flux everywhere else. For $\Delta x \leq 40$ km, the shift to ubiquitous downward flux is complete.

[29] Figure 15 shows a schematic of why this happens. When the tropopause starts to break into filamentary structures, there is typically a bias for material from the stratosphere to extend into the troposphere, with divergent residual flow tending to occur in these structures. At low resolutions, these structures are smoothed out. Therefore the small-scale wind fluctuations stressing the surface of the tropopause can be biased toward positive values due to this decreased surface area. This phenomenon likely depends on the large-scale structure. For example, a bias toward upward flux as low horizontal resolution may exist when a large-scale trough is present in conjunction with a sharp tropopause fold. This would occur since the residual winds would reflect only the larger-scale flow, while neglecting the typically divergent small-scale structure in the fold.

[30] As Δx varies from 40 to 20 km in Figure 14, the maximum in stratosphere to troposphere transport seems to shift toward lower values of L, as well as lower PV surfaces. There also seems to be a significant jump in magnitude below 1.3 PV. Since the troposphere is the source for baroclinic wave activity, it is not surprising that stronger residual motions would be found lower in the stratosphere. In addition, due to decreased stability, the lower-valued PV surfaces are more malleable by wind stresses. We hypothesized that at values of PV less than about 1.2, and with strong wind variations at scales less than 500 km, the material surface is being distorted past the point of irreversiblity. We further hypothesized that at this combination of spatial scale and stability the stressing variations in the wind shift from a "chaotic advection" regime to a self-similar, turbulent cascade. Since the "chaotic advection" regime is responsible for the filamentation of PV, and turbulent enstrophy cascade occurs at, and after, the breakdown of the filaments, it is likely that self-similar turbulent variations in the wind contribute nothing further to irreversible mixing. A further discussion on these hypotheses are given in section 6.2.

[31] Smoothing of the instantaneous flux values (mentioned in section 5.2) had little effect on the total integrated flux values. A comparison at $\Delta x = 40$ of smoothed and unsmoothed flux fields differed by less than 30 percent (not shown), which is well within the range of uncertainty in this kind of calculation in the literature (see next section). Given the results of the previous sections, we surmised that the appropriate parameters to use for flux computations with this method in the type of synoptic situation seen in this case are $\Delta x \sim 30-40$ km, $L_{pr} \sim 400-600$ km and PV $\sim$ 1.3–1.5 PVU.

5.6. Comparison to Other Studies

[32] There have been a number of STE observational and modeling studies performed in recent years, varying in domain size, time frame and horizontal resolution. Table 2 gives just a few of the results of similar studies. (For the purposes of this study, an implicit scaling to flux per unit area per unit time is assumed.) For a 2.5-day simulation over a domain of 9×10^6 km^2, with the ideal parameters, our method results in an ozone flux into the troposphere of around 5×10^{33} molecules, or about 4×10^8 kg, which lies in the range of observed values. *Ebel et al.* [1991] computed, for a similar synoptic situation, but half a day less duration and a third of the domain size a value of 2×10^9 kg. *Lamarque and Hess* [1994] pointed out that Ebel used a sigma surface, rather than a PV surface, for their calculation. With their method computed on the 2 PVU surface (with the same domain as *Ebel et al.* [1991]), and a four-day period, a value of 1.1×10^8 kg was obtained. It is interesting to note that our method, if taken around the 2 PVU surface, results in about 2.3×10^{33} molecules, or about 2×10^8 kg for two and a half days (virtually the same result as *Lamarque and Hess* [1994]). *Ancellet et al.* [1991] found a similar number for an upper limit of ozone transport (2×10^{33} molecules) for a tropopause folding event (about 2.5 days) in their lidar observations.

[33] *Kentarchos et al.* [2000] examined the effects of horizontal resolution on ozone STE in a GCM. Their values, over a much larger domain ($\sim 2 \times 10^7$ km^2), ranged from $5-45 \times 10^{33}$ molecules per day. Given that ozone flux is concentrated in local synoptic storms, the inclusion of two or three more "events" in the same domain easily accounts for some of the higher values. In addition, they calculated ozone mass exchange on a sigma surface, similar to Ebel. *Pierce et al.* [2003] used a regional model over a larger domain ($\sim 2 \times 10^7$ km^2), and a much larger time frame (37 days), with a result of an average ozone downward flux of 0.217 Tg/day. Compared to our study ($\sim$0.127 Tg/day), their domain was slightly more than twice the size, so the values are close to ours. *Hitchman et al.* [2003] used the two-scale method for ozone flux for a convective event during the TRACE-P campaign (24 March) and calculated

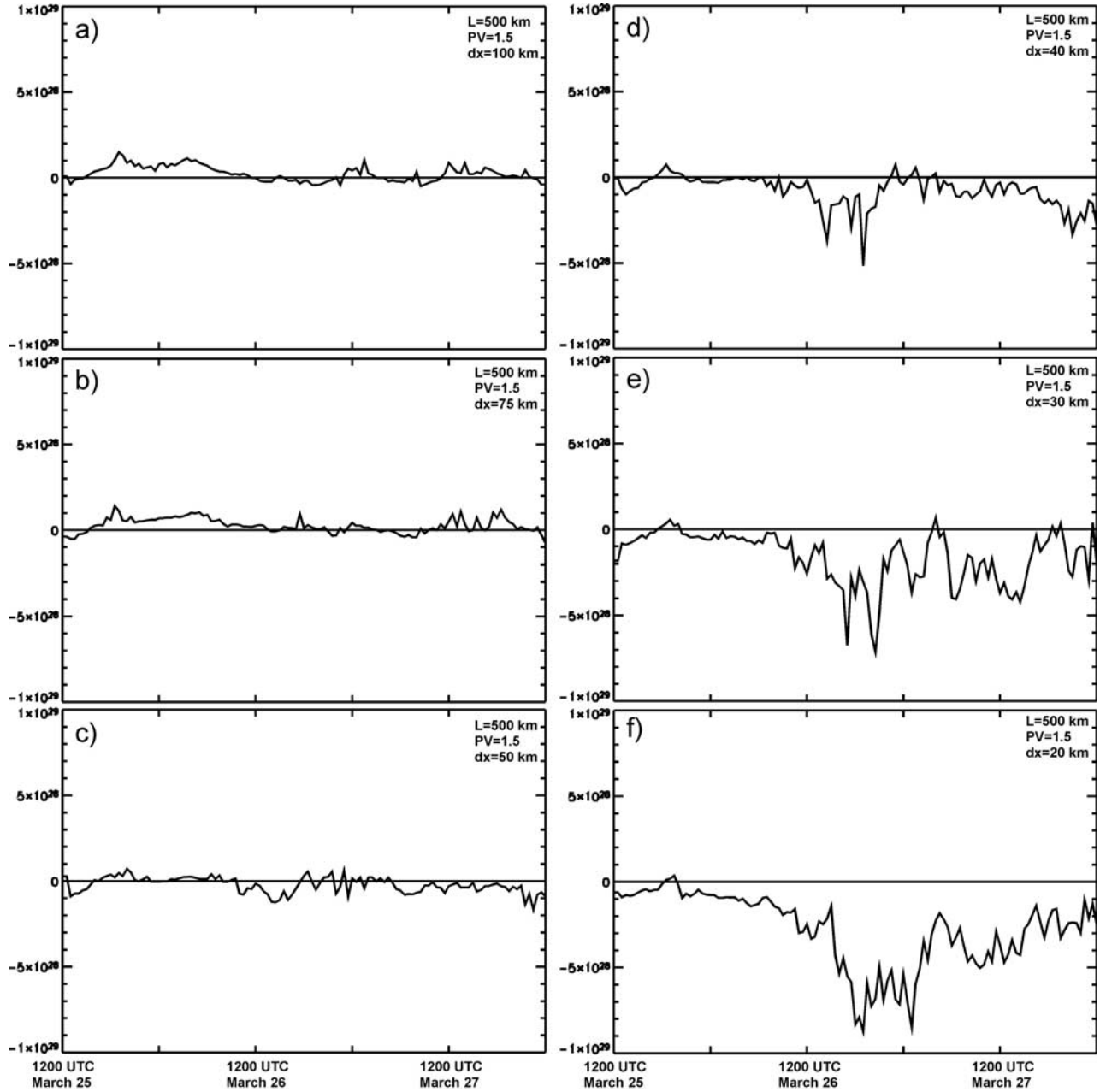

Figure 11. Six-panel plot of domain integrated net flux as a function of time, with horizontal resolutions of (a) 100 km, (b) 75 km, (c) 50 km, (d) 40 km, (e) 30 km, and (f) 20 km.

a value of ~0.7 Tg/day, over a domain of roughly three times the size of this study.

5.7. Flux Divergence of Ozone

[34] Given the strong variation in flux across levels of PV, it is natural to surmise that ozone can flow out of a layer (a PV "slab," for example), where the bottom of the layer is "venting" ozone faster than the top of the layer is "absorbing" it. Eventually, after spreading out the gradient within the layer, this can have the effect of actually sharpening the ozone gradient at the top of the layer. This loss of ozone out of the layer is the result of flux divergence:

$$\frac{dO_3}{dt} \approx -\frac{\partial \overline{\mathbf{F}_{\mathbf{O_3}}}}{\partial Z^*}, \tag{6}$$

where Z^* is a generalized vertical coordinate. For the 20–40-km simulations, most of the flux divergence appears concentrated from 0.9 to 1.6 PVU. By inspection, the amount of ozone flowing out of this layer for the entire simulation ranges from 2×10^{33} molecules at 40 km resolution to 9×10^{33} molecules at 20 km resolution. This calculation, when refined, can provide a baseline in establishing a regional ozone budget for the lowermost stratosphere.

5.8. "Mesoscale Chaotic Kinetic Energy"

[35] It is known that turbulent kinetic energy can enhance irreversible mixing [*Batchelor*, 1949]; by using mixing length theory and eddy diffusion coefficients, one can determine the spatial extent of the mixing taking place.

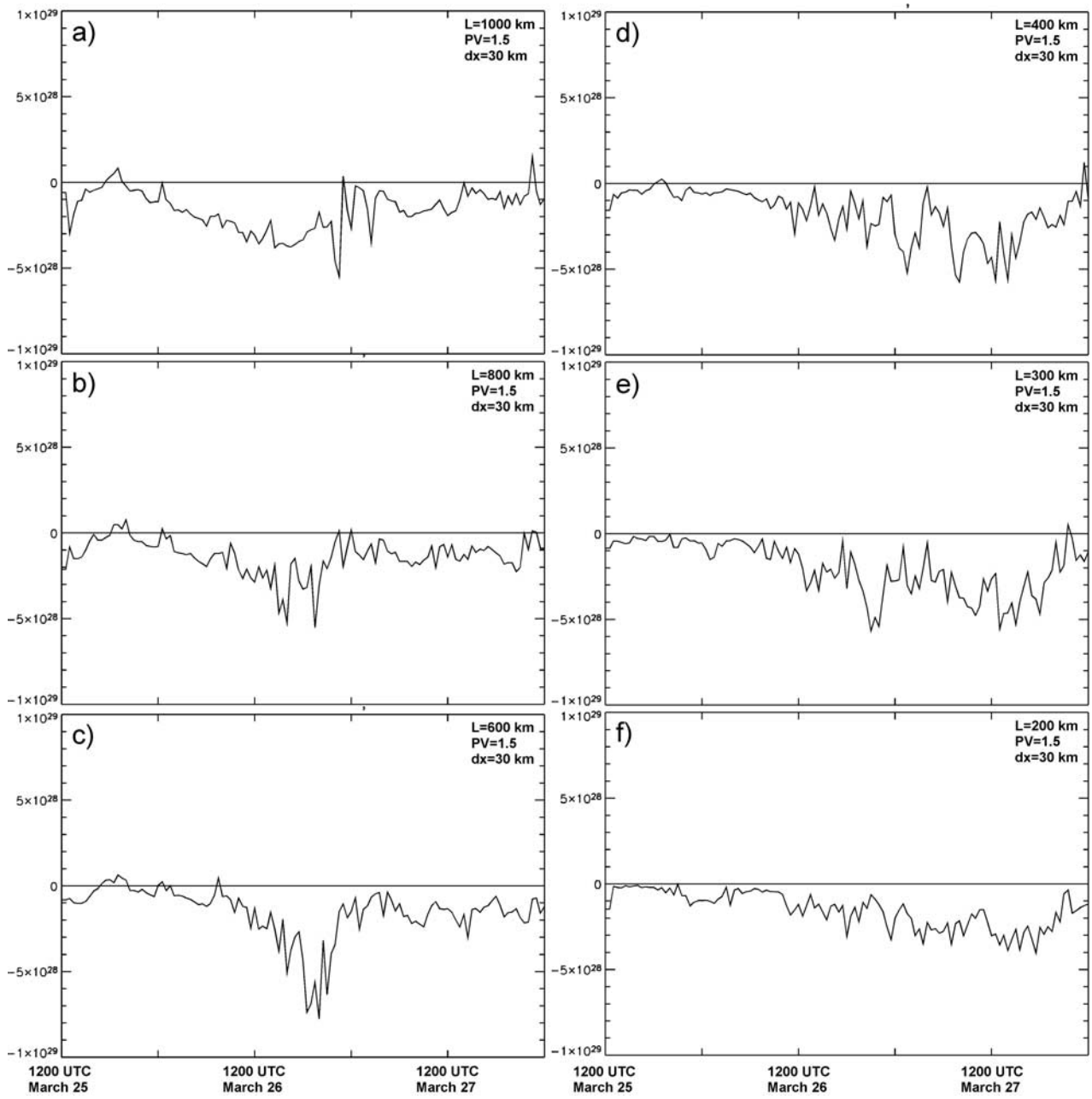

Figure 12. Six-panel plot of spatially integrated net flux as a function of time, calculated with varying spatial scale L_{pr}. L_{pr} = (a) 1000 km, (b) 800 km, (c) 600 km, (d) 400 km, (e) 300 km, and (f) 200 km.

This concept is usually applied to scales much smaller than those emphasized in this study. However, given the scale of the gradients and structures of both PV and ozone, and strong mesoscale fluctuations in the vicinity of these structures, it seems intuitive to refer to a ''mesoscale chaotic kinetic energy'' (MCKE) that can deform a dynamical boundary past the point of reversibility. Gradients in TKE will homogenize constituents locally, yet tend to produce strong anomalies and gradients at the edges of the mixing zone. Regions of resolved mesoscale ''stirring'' near the tropopause could analogously create local anomalies of ozone, and ozone gradients, on the periphery of the MCKE zone. The creation of these local anomalies could be construed as ''flux'' if the zone of MCKE extended across a PV surface. A rough estimate of the relation between flux across a boundary and gradients of mixing could be written as:

$$F \propto \Delta t \nabla \mathbf{u}'^2, \tag{7}$$

where Δt is the model time step.

[36] Figures 16a–16b are plots of MCKE, contours of PV, and areas of smoothed ozone flux. In Figure 16a, a horizontal cross section at about 6 km shows an isolated PV filament along 30°N, 125––140°E, with an area of flux aligned along its breadth. Casual inspection shows the maximum flux occurring on the edges of the local MCKE maxima, while fluxes decrease right at the maxima of

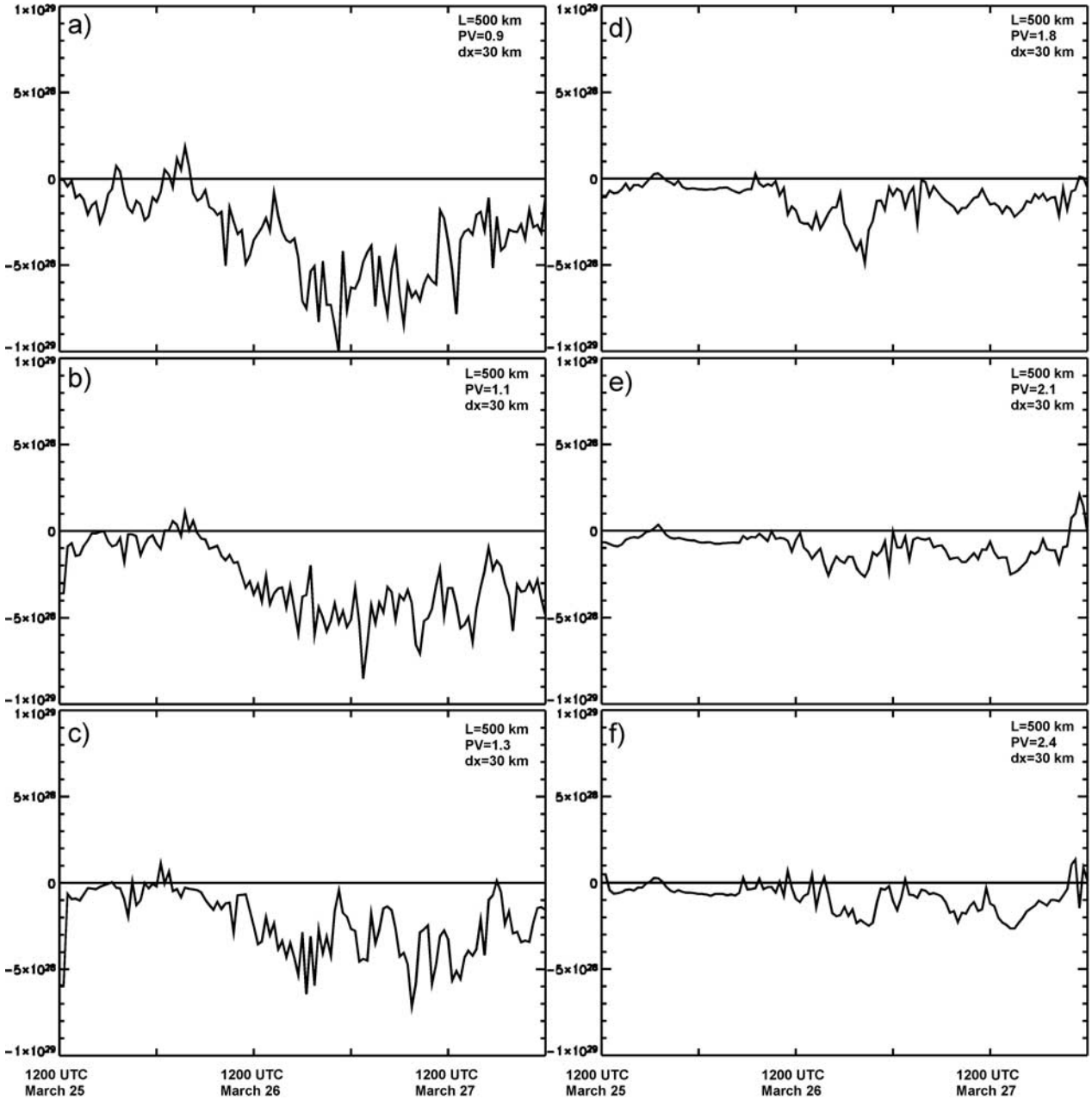

Figure 13. Six-panel plot of spatially integrated net flux as a function of time, calculated at the isosurface of PV = (a) 0.9, (b) 1.1, (c) 1.3, (d) 1.8, (e) 2.1, and (f) 2.4 PVU.

MCKE. A vertical cross section through the maximum (around 135°E, Figure 16b) shows roughly the same relationship, not only at the area of maximum flux but also around other smaller areas of flux. Work toward establishing a more quantitative relationship between MCKE gradients and mixing is in progress.

6. Discussion and Conclusion

[37] The concept of flow "through" the tropopause is difficult to reconcile without diabatic heating, such as latent heat release or radiative heating/cooling, to change the PV on a theta surface. It is known that air parcels can change their PV through local exchange of heat between air parcels undergoing mechanical mixing [*Haynes and Ward*, 1993]. It was the point of this study to investigate and delineate the process of this mixing: where and when the process begins, at what spatial scales, and when the process can be considered "complete." In addition, a broad, three-fold sensitivity study was performed on the new diagnostic to determine the range at which it should be valid. The two-scale method is similar in form to the "perturbation product" flux methodology. In this case, the residual, PV normal wind acts like the perturbation wind, with the fine-scale ozone field being the transported material. However, rather than an actual instantaneous flux, the two-scale approach determines the upper limit mixing potential at any given level, which will be realized more quickly at smaller scales

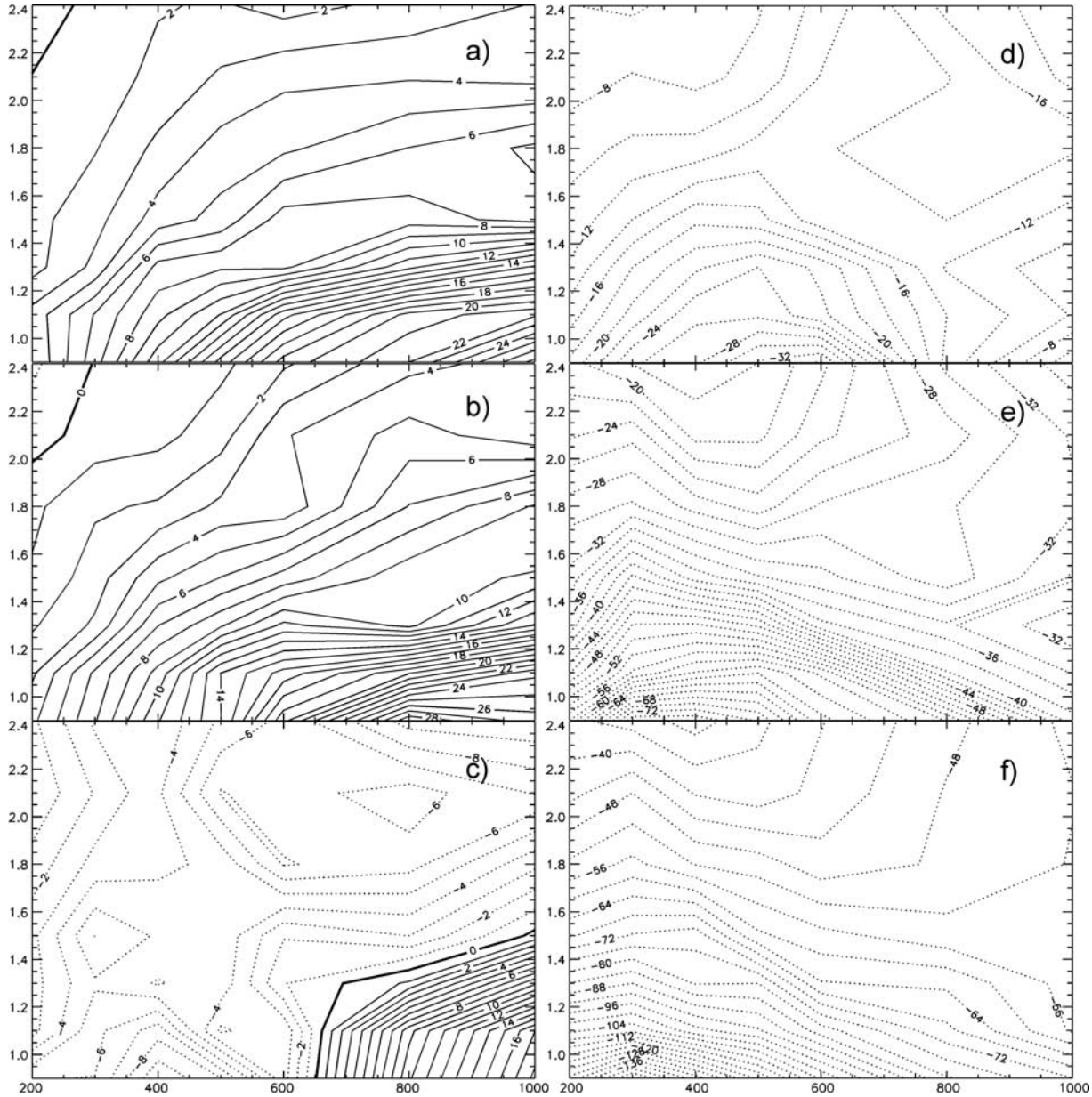

Figure 14. Six-panel contour of spatiotemporally integrated net flux as a function of L_{pr} and PV isosurface in units of 10^{32} molecules O_3, with horizontal resolutions of (a) 100 km, (b) 75 km, (c) 50 km, (d) 40 km, (e) 30 km, and (f) 20 km.

of motion and lower PV (stability) regions. In essence, this method delineates STE due to resolved motions lying in between the model resolution and the tropopause advective scale (L_{pr}). These flux calculations, when taken at typical timescales, PV levels, and spatial scales, have compared well with various other modeling and observational studies of ozone flux across the tropopause.

6.1. Implications for Ozone Budget Calculations

[38] In addition to domain integrated flux agreement with the literature, average local values of flux also compare well, with our method yielding an average value of 25.7 units (1 unit = 1×10^{10} molecules/cm^2–s), while *Kentarchos et al.* [2000] obtains a range of 24.5 to 27.4 units averaged over a ten-day period. Kentarchos et al. further calculated a value of *average* net flux for the entire Northern Hemisphere of around 10 units (higher average values will occur in smaller domains with strong synoptic activity). If we assume a typical spring pattern of about 8–10 major synoptic events in the northern hemisphere at a given time, (our domain captured two in about two days), then our hemispheric value would be 2×10^{33} molecules/day (our average daily value) $\times 10$ (for the other major storms)/86400 (s/day)/5×10^8 km^2/1×10^{10} (cm^2/km^2) = 4.6 units, which compares to 5.7 ± 1.3 by *Beekmann* [1997], and global average values of 1.6–6.4 calculated by *Murphy and Fahey* [1994]. As with Kentarchos et al., values computed during an active spring pattern are assumed to be higher than the annual average. Future work will include a more complete calculation of the total ozone

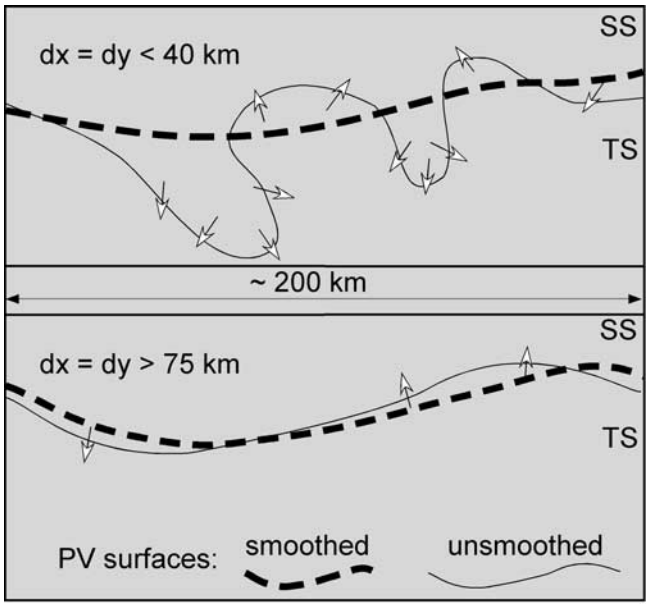

Figure 15. Schematic describing the tendency toward positive flux values at low resolutions using the two-scale method. At higher resolutions (top panel), filamentary structures are well-resolved and typically are biased toward stretching stratospheric air into the troposphere, enhancing downward flux potential. At low resolutions (bottom panel), these structures are absent and the upward bias in flux results.

budget, including the flux divergence out of the lowermost stratosphere.

6.2. Spectral Considerations

[39] It is beyond the scope of this paper to fully interpret the spectral regimes generated by the simulations. However, a theory that the slope of the power spectra can determine the extent of irreversible mixing emerged in this study. It is known that spectral slopes of various atmospheric quantities (e.g., u^2, w^2, T) can characterize the type of flow in certain situations. The -1 power law is sometimes referred to as the "Batchelor regime," which is characterized by "chaotic mixing." This "chaotic mixing" regime differs from turbulent mixing in that there is an external injection of energy into the flow that is driving pure chaotic (incoherent) motion, rather than a cascade of energy or enstrophy upscale or downscale that maintains self-similar coherency. In tracers, a -1 power law is established through extensive filamentation without diffusion. An idealized investigation by *Metais et al.* [1996] showed that the ageostrophic flow in a freely decaying simulation tended toward a -1 slope.

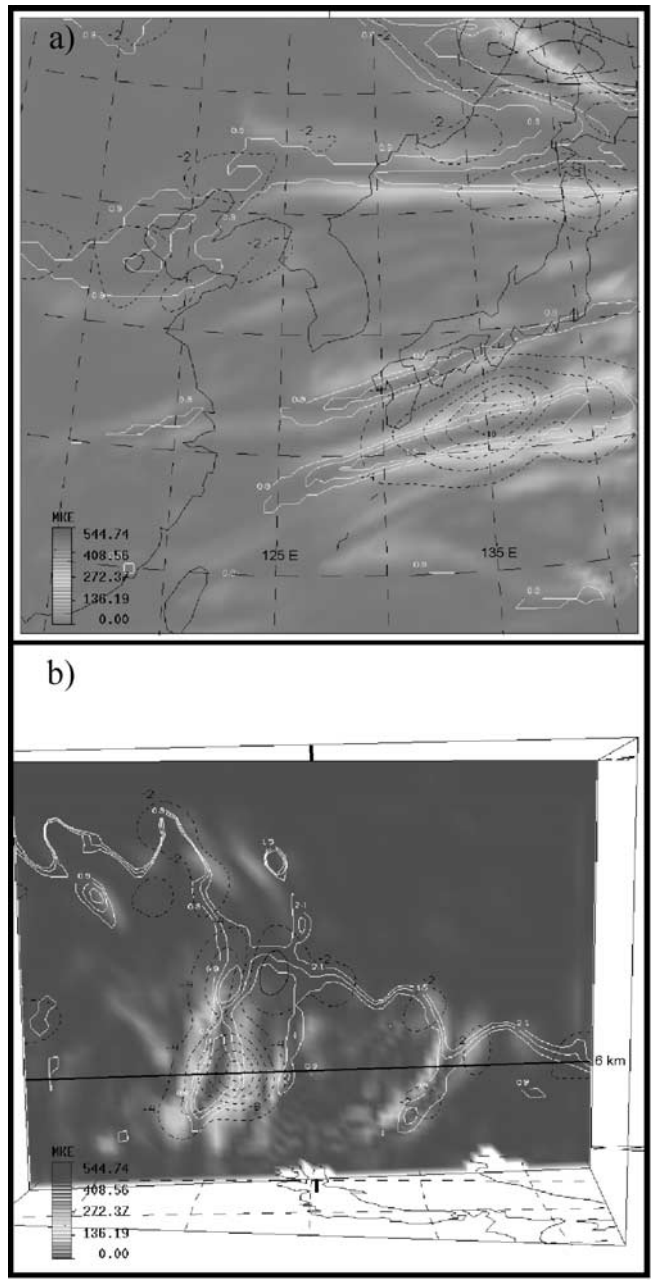

Figure 16. (a) Horizontal cross-section of flux (dash contours, every 2 units), PV (solid contours, every 0.2 PVU from 0.9), and MCKE (color shaded) at z = 6 km. (b) As in Figure 16a, except a westward view of a vertical cross section along roughly 135 E. See color version of this figure at back of this issue.

Table 2. Comparison of Stratospheric-Tropospheric Ozone Transport Studies

Study	Type	Net STT O_3	Domain Size	Duration, days
Ebel et al. [1991]	regional model	2×10^9 kg	3×10^6 km^2	2
Lamarque and Hess [1994]	regional model	1.1×10^8 kg	3×10^6 km^2	4
Kentarchos et al. [2000]	GCM	$5-45 \times 10^8$ kg	2×10^7 km^2	1
Ancellet et al. [1991]	lidar observation	2×10^8 kg	1.5×10^7 km^2	2.5
Pierce et al. [2003]	regional model	8×10^9 kg	2×10^7 km^2	37
Hitchman et al. [2003]	regional model	7×10^8 kg	2.5×10^7 km^2	1
This study	regional model	4×10^8 kg	9×10^6 km^2	2.5

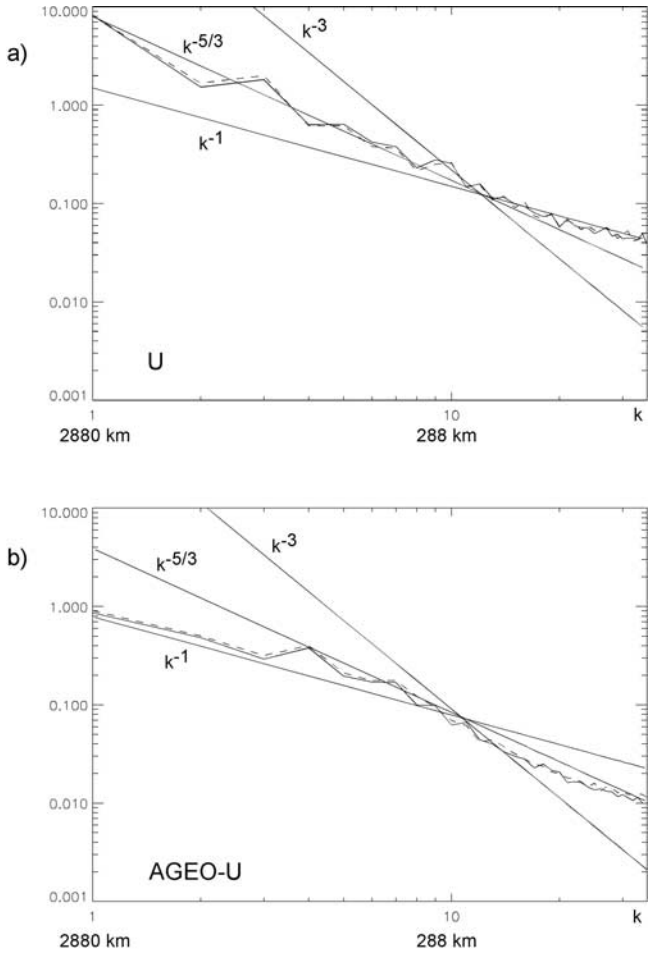

Figure 17. The 3.5-hour average power spectra of (a) zonal wind, and (b) zonal ageostrophic wind (m^2/s^2-km), centered around 1630 UT at PV = 1.3 (dashed) and PV = 0.9 (solid).

Pierrehumbert [1991a] showed that slow, large-scale forcing can drive a −1 power law in the vorticity and tracer fields at much smaller scales. A −3 slope is usually associated with three-dimensional turbulence at small scales, or geostrophic turbulence for wave numbers in the mesoalpha range, both with an enstrophy cascade to higher wave numbers [*Charney*, 1971]. A $k^{-5/3}$ spectrum is typically associated with two-dimensional turbulence, with a reverse energy cascade to lower wave numbers [*Kraichnan*, 1967]. *Nastrom and Gage* [1983] and *Nastrom et al.* [1984], through the Global Atmospheric Sampling program (GASP), deduced that the zonal and meridional winds near the tropopause seem to obey a −5/3 power law for the 2.6–300 km range and a −3 slope for the range 1000–3000 km.

[40] Figure 17a shows the 3.5 hour moving average of UWNMS-generated zonal wind kinetic energy power spectra at the 0.9 (solid) and 1.3 (dashed) PV surfaces at 1630 UT 26 March 26. (The zonal wind is chosen as it comprises the bulk of the energy in both the full and ageostrophic spectrum.) Wave number 10 is approximately 300 km. While the slopes are shallower than what some studies have shown (−5/3 versus −1, −3 versus −5/3), there still is a shift at about 300 km to shallower slope at higher wave numbers. However, the reverse is true for the ageostrophic zonal kinetic energy (Figure 17b), where the spectrum breaks at 300 km to a −1 power law (and sometimes shallower) toward lower wave numbers. *Sadourny* [1974] discussed how at small scales there is an equipartition of energy across divergent modes (leading to a flatter spectrum). Forcing of divergent modes below a certain scale could then trigger this redistribution of energy across the smallest scales. This in turn could force turbulence at those scales. While a firm interpretation of the full and ageostrophic wind power laws cannot be established as of yet, we put the following hypothesis forward.

[41] Ageostrophic motions seem to be largely responsible for deformation of the tropopause [*Hoskins*, 1971; *Keyser and Shapiro*, 1986], and can contribute nearly half the spectral power at mesoscales. Examining the ratio of power of the ageostrophic zonal to the full zonal wind, there tends to be a maximum in contribution from the ageostrophic component in the 300–500 km range, with a slow tailing of influence at larger and smaller scales (not shown). This is consistent with the idea that ageostrophic energy is being injected in the mesoscale range (from geostrophic turbulence). Figure 8b shows a similar plot to Figure 8a, except that the wind vectors are the ageostrophic winds, rather than the residual winds. In this case (and others) the ageostrophic wind seems to line up well with the residual wind necessary for the flux that is diagnosed. It seems possible that the ageostrophic (or residual) wind, feeding off of an external energy injection (baroclinic instability), forces strong divergent modes at smaller scales. That energy is redistributed across even smaller scales and results in a chaotic (flat) power spectrum of the total wind. However, it is hypothesized that at the scale where equipartition of divergent energy dominates, it is also where small-scale, 3-D turbulence begins to occur. It is possible that the turbulent cascade would dominate the ageostrophic spectrum (steepening the slope) while only having a shallow effect on the total wind (−1 slope as opposed to flat). Going one step further, this process could be thought of in the following paradigm: In the vicinity of the lowermost tropopause, the local gradients of PV are contorted by ageostrophic modes to the point of dynamic instability, resulting in turbulent cascade. At this point the ageostrophic spectrum shifts from −1 to −5/3, and it is also where the "stirring" becomes "diffusion." Investigation of the power spectra of the residual winds are part of planned future work.

6.3. Thoughts on PV and Mixing

[42] It is interesting to note that the processes involved in the vicinity of the tropopause can seem to contradict canonical thinking about mixing. Given differential stirring across a layer embedded within a PV (or any) gradient, scalar flux divergence downgradient and out of the layer can eventually result in a *sharper*, rather than a weaker, gradient after the removal of the scalar in the layer, as in the latter hours of case 2 (albeit slowly). This is consistent with the findings of *McIntyre and Palmer* [1984] and *Hitchman et al.* [1999] where baroclinic wave activity acts to "massage the bottom" of the stratosphere, gradually coaxing stratospheric ozone out of the lowest layers while sharpening the PV and ozone gradients above these layers. Thus the areas on the periphery of *greatest* transport have the sharpest

gradients, rather than the gradients being a barrier to transport. *Pierrehumbert* [1991b] raised a similar question of the causality of apparent mixing suppression in the vicinity of sharp PV gradients, especially when advection is chaotic.

6.4. Further Studies

[43] This study seems to have raised more questions on the nature of PV, how it reacts to various stress distributions, and how other studies compare to this new diagnostic. Quantification of mixing rates from MCKE gradients is a current area of new work, in addition to examining the spectral properties of the residual winds and of the flux itself. The method is general and can be applied to STE of water vapor, and other constituents, other synoptic situations [*Hitchman et al.*, 2004], other surfaces besides the tropopause, and constituent budgets in general.

[44] **Acknowledgments.** We thank the TRACE-P science team for their careful measurements, planning, and analysis which made this work possible. We gratefully acknowledge support from NASA TRACE-P grant NCC1-01-011 and ACMAP grant NAG5-11303. We would also like to thank Ted Shepherd for his insightful suggestions.

References

Ancellet, G., et al. (1991), Ground-based lidar studies of ozone exchanges between the stratosphere and the troposphere, *J. Geophys. Res.*, *96*(D12), 22,401–22,421.

Avery, M. A., et al. (2001), Chemical transport across the ITCZ in the central Pacific during an El-Nino–Southern Oscillation cold phase event in March–April 1999, *J. Geophys. Res.*, *106*(D23), 32,539–32,553.

Barnes, S. L. (1973), Mesoscale objective map analysis using weighted time-series observations, *NOAA Tech. Memo. ERL NSSL-69*, 60 pp., Natl. Severe Storms Lab., Norman, Okla.

Barnes, S. L., et al. (1996), Extracting synoptic-scale diagnostic information from mesoscale models: The eta model, gravity waves, and quasigeostrophic diagnostics, *Bull. Am. Meteorol. Soc.*, *77*(3), 519–528.

Batchelor, G. K. (1949), Diffusion in a field of homogeneous turbulence, *Aust. J. Sci. Res.*, *A2*, 437–450.

Beekmann, M. (1997), Regional and global tropopause fold occurrence and related ozone flux across the tropopause, *J. Atmos. Chem.*, *28*(1–3), 29–44.

Browell, E. V., et al. (2003), Large-scale ozone and aerosol distributions, air mass characteristics, and ozone fluxes over the western Pacific Ocean in late winter/early spring, *J. Geophys. Res.*, *108*(D20), 8805, doi:10.1029/2002JD003290.

Charney, J. G. (1971), Geostrophic turbulence, *J. Atmos. Sci.*, *28*, 1087–1095.

Dethof, A., A. O'Neill, and J. Slingo (2000), Quantification of the isentropic mass transport across the dynamical tropopause, *J. Geophys. Res.*, *105*(D10), 12,279–12,293.

Ebel, A., et al. (1991), Simulation of ozone intrusion caused by a tropopause fold and cut-off low, *Atmos. Environ. Part A*, *25*(10), 2131–2144.

Eckman, R. S., W. L. Grose, R. E. Turner, W. T. Blackshear, J. M. Russell III, L. Froidevaux, J. W. Waters, J. B. Kumer, and A. E. Roche (1995), Stratospheric trace constituents simulated by a three-dimensional general circulation model: Comparison with UARS data, *J. Geophys. Res.*, *100*, 13,951–13,966.

Haltiner, G. J., and R. T. Williams (1980), *Numerical Prediction and Dynamical Meteorology*, 2nd ed., John Wiley, Hoboken, N. J.

Haynes, P. H., and W. E. Ward (1993), The effect of realistic radiative-transfer on potential vorticity structures, including the influence of background shear and strain, *J. Atmos. Sci.*, *50*(20), 3431–3453.

Hitchman, M. H., M. L. Büker, and G. J. Tripoli (1999), Influence of synoptic waves on column ozone during Arctic summer 1997, *J. Geophys. Res.*, *104*, 26,547–26,563.

Hitchman, M. H., M. L. Buker, G. J. Tripoli, E. V. Browell, W. B. Grant, T. J. McGee, and J. F. Burris (2003), Nonorographic generation of Arctic polar stratospheric clouds during December 1999, *J. Geophys. Res.*, *108*(D5), 8325, doi:10.1029/2001JD001034.

Hitchman, M. H., M. L. Buker, G. J. Tripoli, R. B. Pierce, J. A. Al-Saadi, E. V. Browell, and M. A. Avery (2004), A modeling study of an east Asian convective complex during March 2001, *J. Geophys. Res.*, *109*, D15S14, doi:10.1029/2003JD004312.

Holton, J. R., P. H. Haynes, M. E. McIntyre, A. R. Douglass, R. B. Rood, and L. Pfister (1995), Stratosphere-troposphere exchange, *Rev. Geophys.*, *33*, 403–439.

Hoskins, B. J. (1971), Atmospheric frontogenesis models—Some solutions, *Q. J. R. Meteorol. Soc.*, *97*(412), 139.

Hoskins, B. J., M. E. McIntyre, and A. W. Robertson (1985), On the use and significance of isentropic potential vorticity maps, *Q. J. R. Meteorol. Soc.*, *111*, 877–946.

Jacob, D. J., J. H. Crawford, M. M. Kleb, V. S. Connors, R. J. Bendura, J. L. Raper, G. W. Sachse, J. C. Gille, L. Emmons, and C. L. Heald (2003), Transport and Chemical Evolution over the Pacific (TRACE-P) aircraft mission: Design, execution, and first results, *J. Geophys. Res.*, *108*(D20), 9000, doi:10.1029/2002JD003276.

Johnson, D. R., T. H. Zapotocny, F. M. Reames, B. J. Wolf, and R. B. Pierce (1993), A comparison of simulated precipitation by hybrid isentropic sigma and sigma models, *Mon. Weather Rev.*, *121*, 2088–2114.

Kentarchos, A. S., G. J. Roelofs, and J. Lelieveld (2000), Simulation of extratropical synoptic-scale stratosphere-troposphere exchange using a coupled chemistry GCM: Sensitivity to horizontal resolution, *J. Atmos. Sci.*, *57*(17), 2824–2838.

Keyser, D., and M. A. Shapiro (1986), A review of the structure and dynamics of upper-level frontal zones, *Mon. Weather Rev.*, *114*(2), 452–499.

Kraichnan, R. H. (1967), Inertial ranges in two-dimensional turbulence, *Phy. Fluids*, *10*, 1417–1423.

Lamarque, J. F., and P. G. Hess (1994), Cross-tropopause mass exchange and potential vorticity budget in a simulated tropopause folding, *J. Atmos. Sci.*, *51*(15), 2246–2269.

McIntyre, M. E., and T. N. Palmer (1984), The surf zone in the stratosphere, *J. Atmos. Terr. Phys.*, *46*(9), 825–849.

Metais, O., et al. (1996), Inverse cascade in stably stratified rotating turbulence, *Dyn. Atmos. Ocean*, *23*(1–4), 193–203.

Murphy, D. M., and D. W. Fahey (1994), An estimate of the flux of stratospheric reactive nitrogen and ozone into the troposphere, *J. Geophys. Res.*, *99*, 5325–5332.

Nastrom, G. D., and K. S. Gage (1983), A first look at wavenumber spectra from GASP data, *Tellus, Ser. A*, *35*(5), 383–388.

Nastrom, G. D., et al. (1984), Kinetic energy spectrum of large scale and mesoscale atmospheric preocesses, *Nature*, *310*(5972), 36–38.

Orlanski, J. (1975), A rational subdivision of scales for atmospheric processes, *Bull. Am. Meteorol. Soc.*, *56*, 527–530.

Pierce, R. B., et al. (2003), Regional Air Quality Modeling System (RAQMS) predictions of the tropospheric ozone budget over east Asia, *J. Geophys. Res.*, *108*(D21), 8825, doi:10.1029/2002JD003176.

Pierrehumbert, R. T. (1991a), Chaotic mixing of tracer and vorticity by modulated traveling Rossby waves, *Geophys. Astrophys. Fluid Dyn.*, *58*(1–4), 285–319.

Pierrehumbert, R. T. (1991b), Large scale horizontal mixing in planetary atmospheres, *Phys. Fluids A*, *3*(5), 1250–1260.

Sadourny, R. (1974), The dynamics of finite-difference models of the shallow-water equations, *J. Atmos. Sci.*, *32*, 680–689.

Shapiro, M. A. (1980), Turbulent mixing within tropopause folds as a mechanism for the exchange of chemical constituents between the stratosphere and troposphere, *J. Atmos. Sci.*, *37*, 994–1004.

Sigmond, M., J. Meloen, and P. Sigmond (2000), Stratosphere-troposphere exchange in an extratropical cyclone, calculated with a Lagrangian method, *Ann. Geophys. Atmos.*, *18*(5), 573–582.

Stohl, A., et al. (2003), Stratosphere-troposphere exchange: A review, and what we have learned from STACCATO, *J. Geophys. Res.*, *108*(D12), 8516, doi:10.1029/2002JD002490.

Tripoli, G. J. (1992a), An explicit three-dimensional nonhydrostatic numerical simulation of a tropical cyclone, *Meteorol. Atmos. Phys.*, *49*, 229–254.

Tripoli, G. J. (1992b), A nonhydrostatic numerical model designed to simulate scale interaction, *Mon. Weather Rev.*, *120*, 1342–1359.

Wei, M. Y. (1987), A new formulation of the exchange of mass and trace consituents between the stratosphere and troposphere, *J. Atmos. Sci.*, *44*(20), 3079–3086.

Wirth, V., and J. Egger (1999), Diagnosing extratropical synoptic-scale stratosphere-troposphere exchange: A case study, *Q. J. R. Meteorol. Soc.*, *125*, 635–655.

M. A. Avery, E. V. Browell, and R. B. Pierce, NASA Langley Research Center, Hampton, VA 23681-2199, USA. (m.a.avery@larc.nasa.gov; e.v.browell@larc.nasa.gov; r.b.pierce@larc.nasa.gov)

M. L. Büker, M. H. Hitchman, and G. J. Tripoli, Department of Atmospheric and Oceanic Sciences, University of Wisconsin-Madison, 1225 W. Dayton, Madison, WI 53706, USA. (marcus@aos.wisc.edu; matt@aos.wisc.edu; tripoli@aos.wisc.edu)

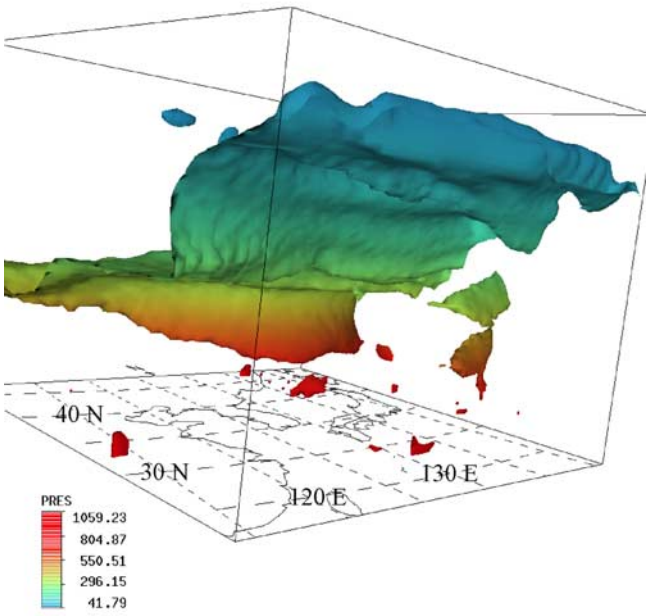

Figure 3. The 1.3 PVU isosurface at 1630 UTC 26 March, viewing from the southwest, colored by pressure (red for higher pressure, blue for lower pressure). Note the dislocated features in the mid-troposphere in the south-eastern quadrant of the domain.

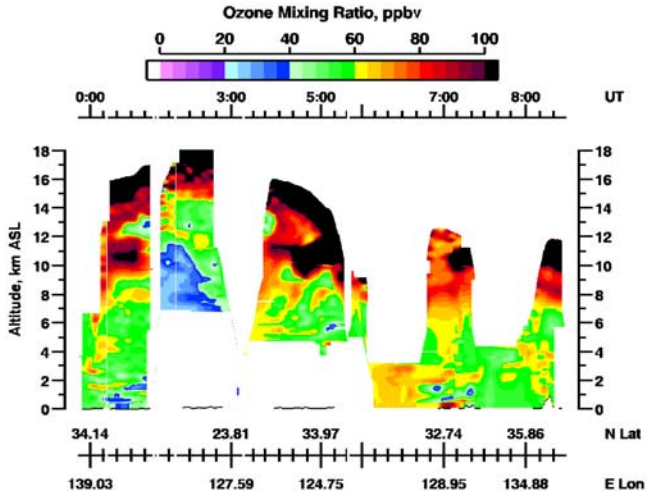

Figure 5. Time-height section of Langley DIAL ozone mixing ratio in ppbv for flight 15. Note the pronounced ozone intrusions at 0000–0100 UT, 0400–0500 UT, and 0700–0800 UT.

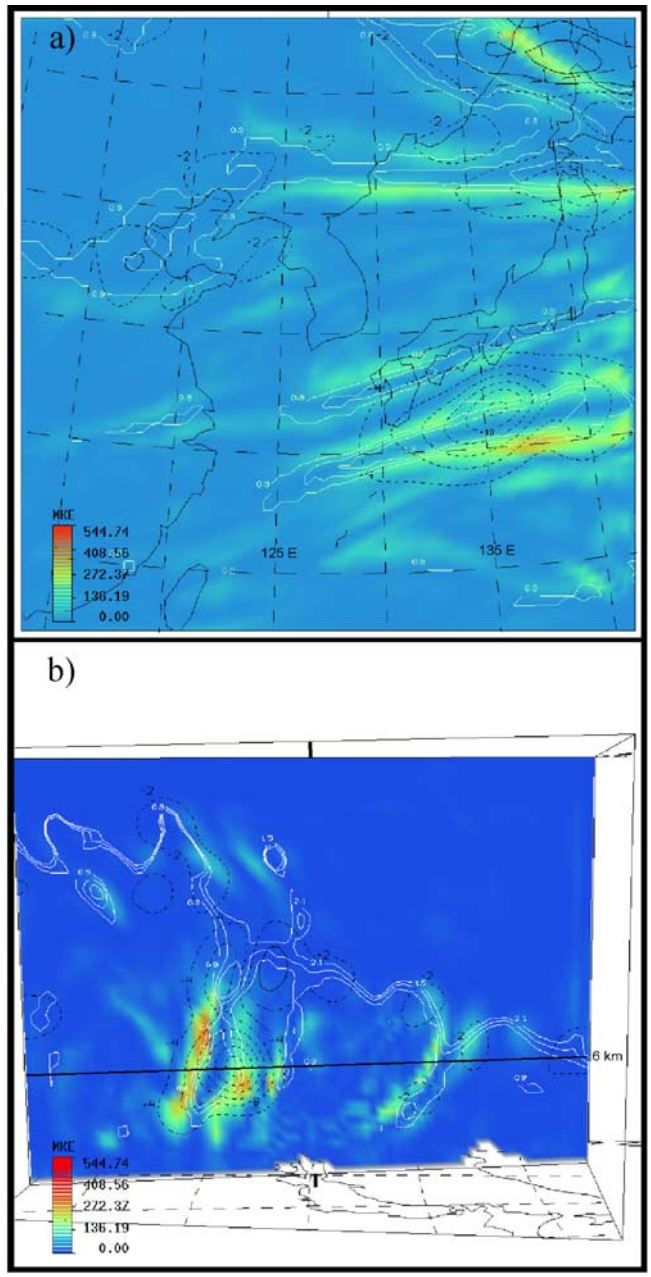

Figure 16. (a) Horizontal cross-section of flux (dash contours, every 2 units), PV (solid contours, every 0.2 PVU from 0.9), and MCKE (color shaded) at z = 6 km. (b) As in Figure 16a, except a westward view of a vertical cross section along roughly 135 E.